Fragmentation analysis of $Z = 112$–116 nuclei using a Skyrme energy density formalism within the collective clusterization approach

Rajni [1,2,*] Kirandeep Sandhu [3,†] and Manoj K. Sharma [2]

[1]*Department of Physics, Sardar Vallabhbhai National Institute of Technology, Surat 395007, Gujarat, India*
[2]*School of Physics and Materials Science, Thapar Institute of Engineering and Technology, Patiala 147004, Punjab, India*
[3]*P.G. Department of Physics, G.S.S.D.G.S Khalsa College, Patiala 147001, Punjab, India*

(Received 3 August 2021; revised 9 December 2021; accepted 4 April 2022; published 25 April 2022)

The Skyrme energy density formalism is applied to address the capture cross sections of $^{286}_{112}$Cn*, $^{292}_{114}$Fl*, and $^{296}_{116}$Lv* superheavy nuclei formed in ^{48}Ca + ^{238}U, ^{244}Pu, ^{248}Cm reactions. The dynamics of ^{48}Ca-induced reactions is investigated by including GSkI and SSk forces for the hot-optimum configurations of decay fragments. The neutron evaporation ($3n$ and $4n$), compound nucleus fission (CN fission) and quasifission (QF) cross sections are calculated with the application of both forces, but the GSkI force seems to be appropriate only for the neutron evaporation channels. However, by including SSk force various decay processes can be handled by including the only parameter of the model, called the neck length parameter (ΔR). The fragment mass distribution of $Z = 112$–116 nuclei shows considerable modifications in the fission, symmetric quasifission ($QF_{sym.}$) and asymmetric quasifission ($QF_{asym.}$) regions with the inclusion of the SSk force as compared to analysis based on the density independent potentials. In addition to this, the role of β_2 deformations and magic shell effects (around the Pb isotope) is scrutinized through the fragmentation behavior and preformation probability of $^{286}_{112}$Cn*, $^{292}_{114}$Fl*, and $^{296}_{116}$Lv* nuclei. Finally, the distribution of the average total kinetic energy of fragments is calculated with the density dependent SSk force and compared with experimental data and earlier work based on the proximity potential.

DOI: 10.1103/PhysRevC.105.044616

I. INTRODUCTION

The study of heavy-ion induced reactions, essential to locate the superheavy island [1], provides a wide range of opportunities to the nuclear community. This has been one of the most challenging tasks for the nuclear world. To study this massive region, the primitive approach of cold fusion reactions [2,3] was undertaken, where ^{208}Pb and ^{209}Bi targets were usually preferred. Although the cold fusion process was quite successful to start in this discipline, it was not sufficient to address the decay cross sections of nuclei with $Z \geqslant 113$. Therefore, a new reaction mechanism based on actinide targets was proposed, called the hot fusion process. These reactions are highly asymmetric in nature and occur at relatively higher excitation energies ($E^*_{CN} =$ 20–50 MeV). Using this process, the elements with $Z =$ 112–118 have been synthesized by using various actinide targets and ^{48}Ca projectile. In such reactions the fusion-evaporation cross sections are observed to be larger than the cross sections calculated in the cold-fusion mechanism (a few picobarns) [4].

In addition to the neutron evaporation in cold and hot fusion approaches, decay processes such as fusion-fission and quasifission are also reported for superheavy nuclei (SHN), which come under the category of compound nucleus (CN) and noncompound nucleus (nCN) decays. If complete equilibrium is attained by the composite system, then the former process is perceived. On the other hand, nCN decay occurs when the system is not equilibrated in all degrees of freedom. Moreover, it is always difficult to distinguish these processes, especially in the case of a symmetric mass split, as the events of symmetric quasifission always compete with the fusion -fission process. Moreover, the contribution of asymmetric quasifission around Pb peaks is also immense. Hence, owing to the large nucleon transfer and energy dissipation, quasifission events (symmetric or asymmetric) are essential to study massive nuclear systems.

In order to address the contribution of the various decay processes of the superheavy nuclei, several theoretical approaches have been developed to understand the reaction dynamics. It is to be noted that in some theoretical formalisms the properties of fission fragments are described in terms of complicated multidimensional potential energy surfaces [5–7]. However, in other theoretical predictions [8–10] the information on low-energy nucleus-nucleus collisions is worked out in terms of the channel coupling effect, which is relevant to understand the compound nucleus and quasifission processes. The contributions of these events towards the reaction crosssections differ by several orders of magnitude, so the parameters (such as mass asymmetry, deformation, energy, radius, etc.) of these models play an important role to address the competing channels. One such model was

*rajni.mittal1989@gmail.com
†kiransndh250@gmail.com

developed by Gupta and collaborators [11–15] and is known as the dynamical cluster-decay model (DCM), which uses the neck-length parameter (ΔR) to account for the experimental data of various decay channels. Owing to this, the aim of the present analysis is precisely based on the deep study of the fragmentation and preformation behaviors [16,17] of $Z = 112$–116 superheavy nuclei formed in $^{48}\mathrm{Ca} + ^{238}\mathrm{U}$, $^{244}\mathrm{Pu}$, and $^{248}\mathrm{Cm}$ reactions [18] within the framework of DCM. Recently Gurjit *et al.* [19] studied the fission properties of the mentioned nuclei, for which the fusion-fission (ff) and asymmetric quasifission ($\mathrm{QF_{asym.}}$) cross sections were calculated using the Blocki based proximity potential [20]. Along with this, different proximity potentials such as Prox-77 [20], Prox-88 [21], and Prox-00 [22] have been used to estimate the experimental average total kinetic energy (TKE). As an extension of [19], the current study is carried out to address the complete capture region, i.e., along with CN-fission (ff) and $\mathrm{QF_{asym.}}$ events, evaporation residue (ER) and symmetric quasifission ($\mathrm{QF_{sym.}}$) processes are also explored. Note that previously [19] the density independent potential [20] was used to investigate the dynamics of $Z = 112$–116 nuclei; however, the present work is extended to address the same within the semiclassical Skyrme energy density formalism (SEDF) [23,24]. In SEDF the density dependent nuclear potential is used, in which spin-saturated and spin-unsaturated components can be separated. Besides this, SEDF has an advantage of using different Skyrme forces which have been applied extensively for heavy ion induced reactions. Out of the numerous Skyrme forces, the GSkI and SSk forces [25] are chosen and the impact of them on capture cross section, mass yield distribution, and average total kinetic energy of decay fragments is worked out. It has been observed that both Skyrme forces (SSk and GSkI) are suitable to address the neutron evaporation ($3n$, $4n$) channels of $^{48}\mathrm{Ca} + ^{238}\mathrm{U}$, $^{244}\mathrm{Pu}$, $^{248}\mathrm{Cm}$ reactions. In contrast, the CN-fission and quasifission cross sections are fitted exclusively through the SSk force. Within the application of SEDF, the mass distribution of $^{286}_{112}\mathrm{Cn}^*$, $^{292}_{114}\mathrm{Fl}^*$, and $^{296}_{116}\mathrm{Lv}^*$ nuclei reveals that asymmetric quasifission ($\mathrm{QF_{asym.}}$) contributes extensively towards the capture cross sections of superheavy nuclei, in addition to the CN fission. Furthermore, the total kinetic energy (TKE) distribution is also modified when the density independent potentials are replaced with the density dependent approach. Broadly speaking, the incorporation of the SSk force lowers the magnitude of the average TKE by 18% for $Z = 112$ and $Z = 114$ nuclei and 14% for the $Z = 116$ nucleus as compared to the previous study [19]. Owing to the above discussion, the main emphasis of the present analysis is that (1) to see the effect of different Skyrme forces on the capture cross section of $^{48}\mathrm{Ca} + ^{238}\mathrm{U}$, $^{244}\mathrm{Pu}$, $^{248}\mathrm{Cm}$ reactions and (2) to study the mass distribution and average TKE patterns using the SEDF approach.

The paper is organized as follows: the methodology, which includes the framework of the dynamical cluster decay model (DCM) and the Skyrme energy density formalism, is presented in Sec. II. Calculations and results are discussed in Sec. III, and finally the outcomes are summarized in Sec. IV.

II. METHODOLOGY

A. Skyrme energy density formalism (SEDF)

In the Skyrme energy density formalism (SEDF), the nuclear interaction potential $V_N(R)$ between two colliding nuclei is defined as

$$V_N(R) = E_{\mathrm{tot}}(R) - E_1 - E_2, \tag{1}$$

where $E_{\mathrm{tot}}(R)$ is the total energy expectation value of the colliding parters at distance R (center to center), and the individual energies of noninteracting projectile and target nuclei are represented by E_1 and E_2. The energy expectation values $E_{\mathrm{tot}}(R)$, E_1, and E_2 are obtained by volume integration of the Hamiltonian density $H(\vec{r})$ as

$$E_{\mathrm{tot}}(R) = \int H[\rho_p(\vec{r}), \rho_n(\vec{r})]d\vec{r}, \tag{2}$$

$$E_i(R) = \int H[\rho_{ip}(\vec{r}), \rho_{\mathrm{in}}(\vec{r})]d\vec{r} \quad (i = 1, 2), \tag{3}$$

Here $\rho_{ip}(\vec{r})$, $\rho_{\mathrm{in}}(\vec{r})$ are proton and neutron densities of noninteracting nuclei and $\rho_p(\vec{r})$, $\rho_n(\vec{r})$ are densities of interacting nuclei. $H(\vec{r})$ in the above equation stands for the energy density functional as given in [23], including the kinetic energy contribution τ(r) and nuclear interaction parts $H_{\mathrm{sky}}(\vec{r})$,

$$H(\rho, \tau, \vec{J}) = \frac{\hbar^2}{2m}\tau + H_{\mathrm{sky}}(\vec{r}). \tag{4}$$

The kinetic energy density τ is then calculated by the extended Thomas fermi approximation of Bartel *et al.* [26].

In Eq. (4), the Skyrme Hamiltonian is given by

$$\begin{aligned}
H_{\mathrm{sky}}(\vec{r}) = {} & \frac{1}{2}t_0\left[\left(1+\frac{1}{2}x_0\right)\rho^2 - \left(x_0+\frac{1}{2}\right)\left(\rho_n^2+\rho_p^2\right)\right] \\
& + \frac{1}{2}\sum_{i=1}^{3} t_{3i}\rho^{\alpha_i}\left[\left(1+\frac{1}{2}x_{3i}\right)\rho^2 - \left(x_{3i}+\frac{1}{2}\right)\right. \\
& \left.\times\left(\rho_n^2+\rho_p^2\right)\right] + \frac{1}{4}\left[t_1\left(1+\frac{1}{2}x_1\right)+t_2\left(1+\frac{1}{2}x_2\right)\right]\rho\tau \\
& - \frac{1}{4}\left[t_1\left(x_1+\frac{1}{2}\right) - t_2\left(x_2+\frac{1}{2}\right)\right](\rho_n\tau_n + \rho_p\tau_p) \\
& + \frac{1}{16}\left[3t_1\left(1+\frac{1}{2}x_1\right) - t_2\left(1+\frac{1}{2}x_2\right)\right](\vec{\nabla}\rho)^2 \\
& - \frac{1}{16}\left[3t_1\left(x_1+\frac{1}{2}\right) + t_2\left(x_2+\frac{1}{2}\right)\right] \\
& \times\left[(\vec{\nabla}\rho_n)^2 + (\vec{\nabla}\rho_p)^2\right] \\
& + \frac{1}{2}W_0[\rho\vec{\nabla}\cdot\vec{J} + \rho_n\vec{\nabla}\cdot\vec{J}_n + \rho_p\vec{\nabla}\cdot\vec{J}_p] \\
& - \left[\frac{1}{16}(t_1x_1+t_2x_2)\vec{J}^2 - \frac{1}{16}(t_1-t_2)\left(\vec{J}_p^2+\vec{J}_n^2\right)\right],
\end{aligned} \tag{5}$$

where the nuclear and spin-orbit densities are represented by ρ and $\vec{J}$. t_j, x_j $(j = 0, 1, 2)$, t_{3i}, x_{3i}, α_i $(i = 1, 2, 3)$, and W_0 represent various Skyrme parameters. The last term in the Hamiltonian represents the tensor coupling component where spin and gradient contributions are included. Agarwal *et al.*

TABLE I. Parameter sets of GSkI and SSk Skyrme forces, taken from [25].

Parameter	Force	
	GSkI	SSk
t_0 (MeVfm^3)	−1855.45	−2523.52
t_1 (MeV fm^5)	397.23	435.0
t_2 (MeV fm^5)	264.63	−382.04
t_{31} (MeV fm$^{3(\alpha_1+1)}$)	2309.67	2372.49
t_{32} (MeV fm$^{3(\alpha_2+1)}$)	−449.01	0.0
t_{33} (MeV fm$^{3(\alpha_3+1)}$)	−53.31	0.0
x_0	0.1180	0.6835
x_1	−1.7586	−0.4519
x_2	−1.8068	−0.9214
x_{31}	0.1261	1.0508
x_{32}	−1.1881	0.0
x_{33}	−0.4594	0.0
α_1	$\frac{1}{3}$	$\frac{1}{6}$
α_2	$\frac{2}{3}$	0.0
α_3	1	0.0
W_0 (MeV fm^5)	169.57	131.98

[25] have proposed some new Skyrme forces based on the generalized Skyrme effective force (GSEF) procedure, named GSkI and GSkII, and others based on the standard Skyrme effective force (SSEF), such as the SSk force. The difference in these forces is the contribution to the density dependence in second term of the Hamiltonian. GSkI includes density-dependent terms proportional to ρ^{α_i} with $\alpha_i = 1/3, 2/3$, and 1, while for the SSk force $\alpha_i = \alpha_1 = 1/6$. Moreover in the GSkI force the density dependence is specified by six parameters namely, t_{3i} and x_{3i} with $i = 1$, 2, and 3, whereas in the SSk force, only three parameters are used, t_{31}, x_{31}, and α_1. In this work we have used GSkI and SSk forces, which are found to account better at near barrier energies [27]. The parameters of both the Skyrme forces are shown in Table I.

In Eq. (5), the spin $\vec{J}$ is a purely quantal property, and hence has no contribution in the lowest Thomas-Fermi (TF) order. However, at the Extended Thomas Fermi (ETF) level, the second-order contribution gives

$$\vec{J}_q(\vec{r}) = -\frac{2m}{\hbar^2}\frac{1}{2}W_0\frac{1}{f_q}\rho_q\vec{\nabla}(\rho+\rho_q), \tag{6}$$

with f_q as the effective-mass form factor,

$$f_q(\vec{r}) = 1 + \frac{2m}{\hbar^2}\frac{1}{4}\left\{t_1\left(1+\frac{x_1}{2}\right) + t_2\left(1+\frac{x_2}{2}\right)\right\}\rho(\vec{r}) - \frac{2m}{\hbar^2}\frac{1}{4}\left\{t_1\left(x_1+\frac{1}{2}\right) - t_2\left(x_2+\frac{1}{2}\right)\right\}\rho_q(\vec{r}). \tag{7}$$

Note that each of τ_q, f_q, and $\vec{J}_q$ are functions of ρ_q and/or ρ alone.

The densities of the composite system, $\rho = \rho_1 + \rho_2$ with $\rho_i = \rho_{\rm in} + \rho_{ip}$ $(i = 1, 2)$, and the $\tau(\rho)$ and $\vec{J}(\rho)$ are added under the frozen density approximation, as follows:

$$\tau(\rho) = \tau_1(\rho_1) + \tau_2(\rho_2), \qquad \vec{J}(\rho) = \vec{J}_1(\rho_1) + \vec{J}_2(\rho_2), \tag{8}$$

with $\rho_i = \rho_{\rm in} + \rho_{ip}$, $\tau_i(\rho_i) = \tau_{\rm in}(\rho_{\rm in}) + \tau_{ip}(\rho_{ip})$, and $\vec{J}_i(\rho_i) = \vec{J}_{\rm in}(\rho_{\rm in}) + \vec{J}_{ip}(\rho_{ip})$.

For nuclear density ρ_i of each nucleus, the temperature dependent two-parameter Fermi density (FD) distribution for the slab approximation is given by [28].

B. The dynamical cluster-decay model (DCM)

The dynamical cluster-decay model (DCM) finds its genesis in the quantum mechanical fragmentation theory (QMFT) [29–31]. This methodology is described in terms of a few coordinates: (i) the collective coordinates of mass (and charge) asymmetry $\eta = (A_1 - A_2)/(A_1 + A_2)$ [and $\eta_Z = (Z_1 - Z_2)/(Z_1 + Z_2)$], (ii) relative separation R, (iii) the collective surface co-ordinates or simply deformations $\beta_{\lambda i}$ and orientations θ_i $(i = 1, 2)$ of two nuclei.

In DCM, the compound nucleus (CN) decay cross sections in terms of partial waves analysis are defined as

$$\sigma = \sum_{\ell=0}^{\ell_{\rm max}}\sigma_\ell = \frac{\pi}{k^2}\sum_{\ell=0}^{\ell_{\rm max}}(2\ell+1)P_0^\ell P_\ell, \quad k = \sqrt{\frac{2\mu E_{\rm c.m.}}{\hbar^2}} \tag{9}$$

where $\mu = \frac{A_1A_2}{A_1+A_2}m$ is the reduced mass and m is the nucleon mass. The preformation probability P_0^ℓ is calculated within the collective clusterization method (in reference to to η motion) and penetrability P_ℓ is worked out in reference to the R motion. In the collective clusterization process, the relative preformation probability of all possible binary fragments is taken into account. $\ell_{\rm max}$ is the maximum angular momentum, fixed in reference to the sustainability of the light particle cross section i.e., $\sigma_{\rm ER}(\ell) \to 0$ at $\ell = \ell_{\rm max}$.

P_0^ℓ for each ℓ is calculated by solving the stationary Schrödinger equation in η, at a fixed R:

$$\left[-\frac{\hbar^2}{2\sqrt{B_{\eta\eta}}}\frac{\partial}{\partial\eta}\frac{1}{\sqrt{B_{\eta\eta}}}\frac{\partial}{\partial\eta} + V(\eta, T)\right]\psi^\nu(\eta) = E_\eta^\nu\psi^\nu(\eta), \tag{10}$$

where, $\nu = 0, 1, 2, \ldots$ represent the ground state ($\nu = 0$) and excited state solutions.

The penetrability P_ℓ is estimated using the Wentzel-Kramers-Brillouin (WKB) integral

$$P_\ell = \exp\left[-\frac{2}{\hbar}\int_{R_a}^{R_b}\{2\mu[V(R) - Q_{\rm eff}]\}^{1/2}dR\right], \tag{11}$$

with $V(R_a, T) = V(R_b, T) = {\rm TKE}(T) = Q_{\rm eff}$, where $V(R_a)$ and $V(R_b)$ represent the potentials at entry and exit points of the barrier and TKE and $Q_{\rm eff}$ refer to total kinetic energy and effective Q value of the decay process. The temperature T is related to the incoming center-of-mass energy $E_{\rm c.m.}$ or the compound nucleus excitation energy $E^*_{\rm CN}$ via the entrance channel $Q_{\rm in}$ value as [32]

$$E^*_{\rm CN} = E_{\rm c.m.} + Q_{\rm in} = aT^2 - T \quad (T \text{ in MeV}), \tag{12}$$

$Q_{\rm in} = B_1 + B_2 - B_{\rm CN}$, with binding energies B taken from [33,34]. We have used $a = A_{\rm CN}/11$ in this work, where $A_{\rm CN}$ is the mass of the compound nucleus.

The entry point of the scattering potential reads

$$R_a(\alpha_1, \alpha_2, T) = R_1(\alpha_1, T) + R_2(\alpha_2, T) + \Delta R(\eta, T) = R_t(\alpha_1, \alpha_2, T) + \Delta R(\eta, T), \quad (13)$$

The radii for two deformed nuclei are given as

$$R_1(\alpha_1, T) = R_{01}(T)\left[1 + \sum_\lambda \beta_{\lambda 1} Y_\lambda^{(0)}(\alpha_1)\right],$$
$$R_2(\alpha_2, T) = R_{02}(T)\left[1 + \sum_\lambda \beta_{\lambda 2} Y_\lambda^{(0)}(\alpha_2)\right] \quad (14)$$

with half density radii (R_{01} and R_{02}) obtained by fitting the experimental data for mass region $A = 4$–238 [35,36]. This radius parameter has been tested for superheavy system also with mass $A_{\rm CN} = 266$ [37], and the same value is used in the present work to study the decay properties of heavier SHN with $A_{\rm CN} = 286$, 292, and 296. However, it will be of future interest to employ a more appropriate radius parameter for such analysis. In Eq. (13), ΔR refers to the neck-length parameter which assimilates the neck formation effects as taken in the asymmetric two-center shell model (ATCSM) [29]. α_1 (and α_2) is an angle that the radius vector R_1 (and R_2) of the colliding nuclei makes with the symmetry axis, measured clockwise.

The compound nucleus excitation energy $E^*_{\rm CN}$ gets distributed into total excitation energy TXE and total kinetic energy TKE of the two outgoing fragments at each T as $E^*_{\rm CN} + Q_{\rm out}(T) = {\rm TKE}(T) + {\rm TXE}(T)$. Then the exit channel fragments can be obtained in the ground state with ${\rm TKE}(T = 0)$ $[= Q_{\rm out}(T = 0)]$ by allowing the emission of light particles and/or γ rays with an energy $E_x = Q_{\rm eff}(T) - Q_{\rm out}(T = 0) = {\rm TKE}(T) - {\rm TKE}(T = 0)$ such that the remaining excitation energy of the decaying system is $[E^*_{\rm CN} + Q_{\rm out}(T)] - E_x = {\rm TKE}(T = 0) + {\rm TXE}(T)$. The TXE(T) is used in secondary particle emission of light particles from the primary fragments, but those are not treated here; instead we compare our calculations with primary, presecondary evaporation fragment emission data. Moreover, the average ${\rm TKE}(T)$ can be defined as $\langle {\rm TKE}\rangle = \sum_{\ell=0}^{\ell_{\rm max}} \frac{\sigma_\ell(A_2)}{\sigma(A_2)} {\rm TKE}(\ell, A_2)$. For every fragment, the TKE for each ℓ is averaged over its corresponding production cross section σ_ℓ with respect to total cross section $\sigma(A_2) = \sum_{\ell=0}^{\ell_{\rm max}} \sigma_\ell(A_2)$.

The deformation and orientation dependent fragmentation potential used in Eq. (10), at any temperature T, is given by

$$V(\eta, R, \beta_{\lambda 1}, \beta_{\lambda 2}, \theta_1, \theta_2, T) = \sum_{i=1}^{2} V_{\rm LDM}(A_i, Z_i, T) + \sum_{i=1}^{2} \delta U_i \exp\left(-\frac{T^2}{T_0^2}\right) + V_C(R, Z_1, Z_2, \beta_{\lambda 1}, \beta_{\lambda 2}, \theta_1, \theta_2, T) + V_N(R, A_1, A_2, \beta_{\lambda 1}, \beta_{\lambda 2}, \theta_1, \theta_2, T) + V_\ell(R, A_1, A_2, \beta_{\lambda 1}, \beta_{\lambda 2}, \theta_1, \theta_2, T). \quad (15)$$

The first two terms appearing in above equation form binding energies (BEs) of nuclei, taken from the experimental data of Audi Wapstra [33]. Wherever the experimental BEs are not given, the theoretical BEs of Möller *et al.* [34] are used. The BE is the sum of the liquid drop model energy $V_{\rm LDM}$ of Davidson *et al.* [38] and "empirical" shell corrections δU of Myers and Swiatecki [39]. V_C, V_ℓ, and V_N are the temperature dependent Coulomb, centrifugal, and nuclear potentials of two decaying fragments having mass and charge numbers A_i and Z_i $(i = 1, 2)$ respectively. It is important to note that nuclear potential V_N is calculated by using the Skyrme energy density formalism (SEDF) (discussed in Sec. II A).

III. RESULTS AND DISCUSSION

In this section, the decay of ^{286}Cn* (Z = 112), ^{292}Fl* (Z = 114) and ^{296}Lv* (Z = 116) nuclei is studied by using the Skyrme based density dependent nuclear potential. The SSk and GSkI Skyrme forces are used to understand the dynamics of actinide-based hot fusion reactions. The present investigation is divided into two sections. In section A, the capture cross sections which is the sum of neutron evaporation, fusion-fission and quasi-fission are calculated within the center-of mass energy range $E_{\rm c.m.} = 195-206$ MeV using Skyrme forces. The yield of the decay fragments in terms of preformation probability (or fragment mass yield P_0) is calculated in order to look for the competing processes involved in decay of Z = 112–116 nuclei. Subsequent to this, the compound nucleus formation probability ($P_{\rm CN}$) of the considered superheavy nuclei (SHN) is estimated within the fixed range of the neck-length parameter. Section B is devoted to address the average total kinetic energy $\langle {\rm TKE}\rangle$ of fission and quasi-fission fragments observed in the collective clusterization process.

A. Role of Skyrme forces in the capture cross sections

To see the effect of SSk and GSkI Skyrme forces on the barrier characteristics [V_B, R_B, $V(R_a)$ and R_a], Fig. 1 is plotted for the ^{286}Cn* composite system decaying into ^{48}Ca + ^{238}U fragments at center-of-mass energy $E_{\rm c.m.} = 199.04$ MeV and $\ell = 75\hbar$. With the use of two different Skyrme forces the following changes in reference to barrier characteristics are observed:

(i) The decay barrier height (V_B) for the ^{48}Ca + ^{238}U channel is calculated as 196.59 and 193.60 MeV respectively with GSkI and SSk forces.
(ii) The value of the barrier position (R_B) is observed to be 13.32 and 13.59 fm respectively for GSkI and SSk forces.
(iii) The calculated potential at first turning point, $V(R_a)$ (and radius R_a) (marked in Fig. 1) of the barrier is 193.54 MeV ($R_a = 12.97$ fm) for the GSkI force, which shows a decrement of ∼3 MeV from the SSk Skyrme force (190.69 MeV, 12.72 fm).

This indicates that the barrier characteristics show visible change with the chosen Skyrme forces. It is important to mention that in the recent past the decay analysis of ^{286}Cn nucleus

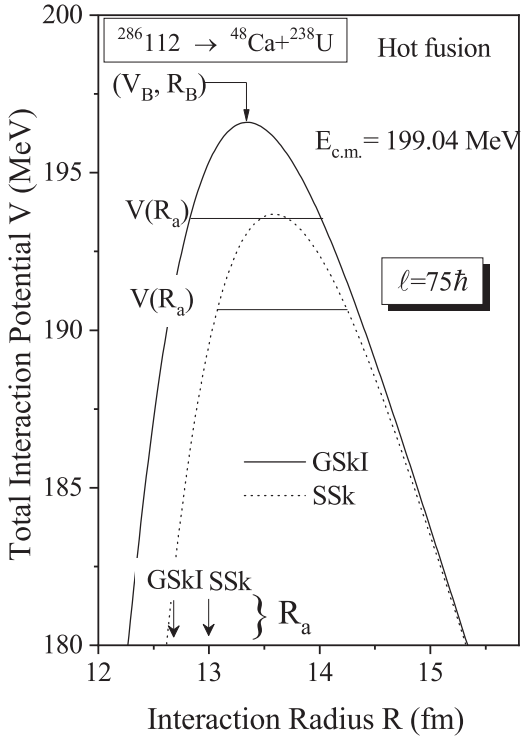

FIG. 1. Variation of total interaction potential V (MeV) as a function of internuclear radius R for the decay of ^{286}Cn* into ^{48}Ca + ^{238}U plotted with GSkI and SSk Skyrme forces.

was carried out using the Prox-77 potential [19]. However, the present figure is plotted by including the SEDF approach, and the comparison of Skyrme based potentials and Prox-77 reveals the fact that a higher magnitude of barrier height is measured with the Prox-77 potential, which gets mitigated in GSkI, and relatively lower magnitude is observed for SSk force. Hence, the barrier characteristics are significantly modified when the Prox-77 potential is replaced by the density dependent Skyrme potential.

The impact of SSk and GSkI forces is further investigated in the fragmentation potential V (MeV), plotted for the decay of ^{286}Cn*, ^{292}Fl*, and ^{296}Lv* nuclei in Fig. 2. The figures for $Z = 112$, 114, and 116 nuclei are presented at the highest center-of-mass energies along with the maximum angular momentum state. It is observed from Figs. 2(a)–2(c) that for the chosen nuclear systems, irrespective of the difference in magnitude of the fragmentation potential, the structure of potential energy surface remains almost identical with both Skyrme forces. It is worth mentioning that the lowest magnitude of fragmentation potential is obtained for the heavy mass fragment (HMF) ranges $A_2 = 73$–82, $A_2 = 79$–90, and $A_2 = 80$–97 respectively for ^{286}Cn*, ^{292}Fl*, and ^{296}Lv* nuclei. However, the intermediate mass fragments (IMFs) ranging from $5 \leqslant A \leqslant 20$ are the least probable decaying candidates, attributed to the highest fragmentation potential. The difference in the structure of the fragmentation potential is further rectified by probing the behavior of two input variables of the DCM: (i) the effect of deformations (included up to β_2) and (ii) the role of the shell corrections for decaying fragments (particularly the Pb magicity), the results of which are shown in Fig. 3.

Figure 3(a) is plotted to explore the influence of deformations (up to β_2) on the decay path of the $Z = 112$ nucleus using SSk and GSkI forces. The fragmentation potential for the spherical approach is also included in the same figure (for SSk force only) to look for the changes in the fragmentation structure due to β_2 deformations. It is clear from Fig. 3(a) that the fragmentation potential with spherical choice of nuclei is

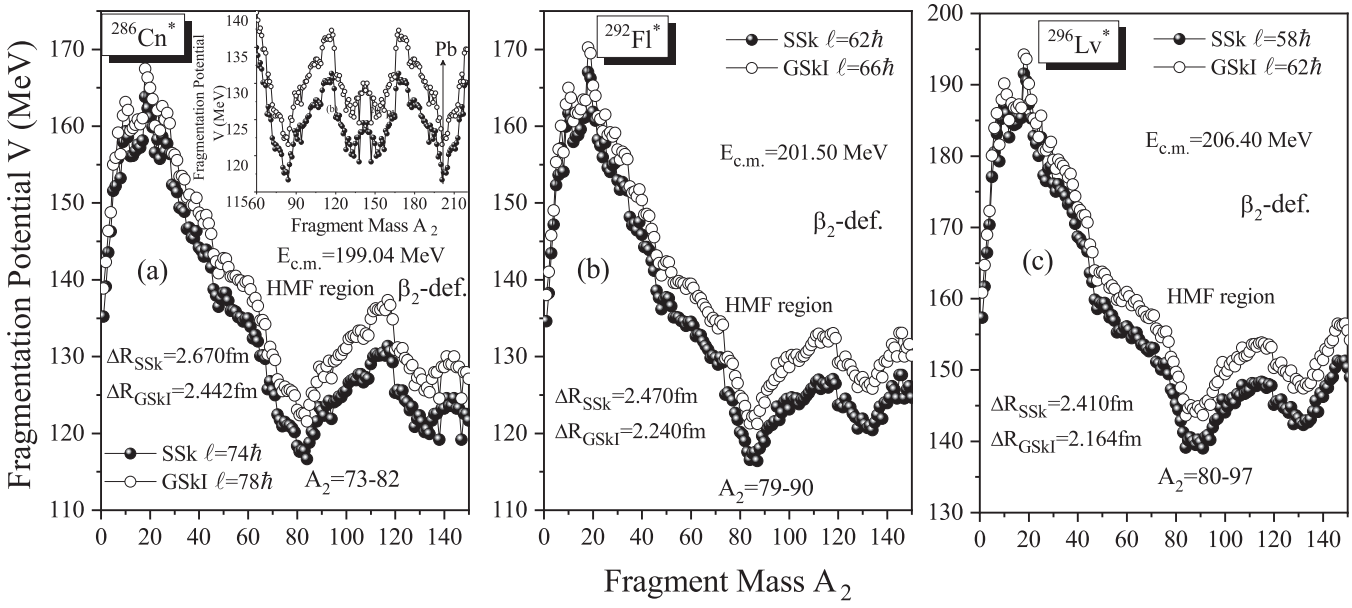

FIG. 2. Fragmentation potential plotted as a function of fragment mass (A_2) for (a) ^{286}Cn*, (b) ^{292}Fl*, and (c) ^{296}Lv* superheavy nuclei with GSkI and SSk Skyrme forces. The inset shows the fragmentation graph for the complete mass region for the ^{286}Cn* nucleus. The variation is presented at the highest magnitude of the center-of-mass energy in this figure.

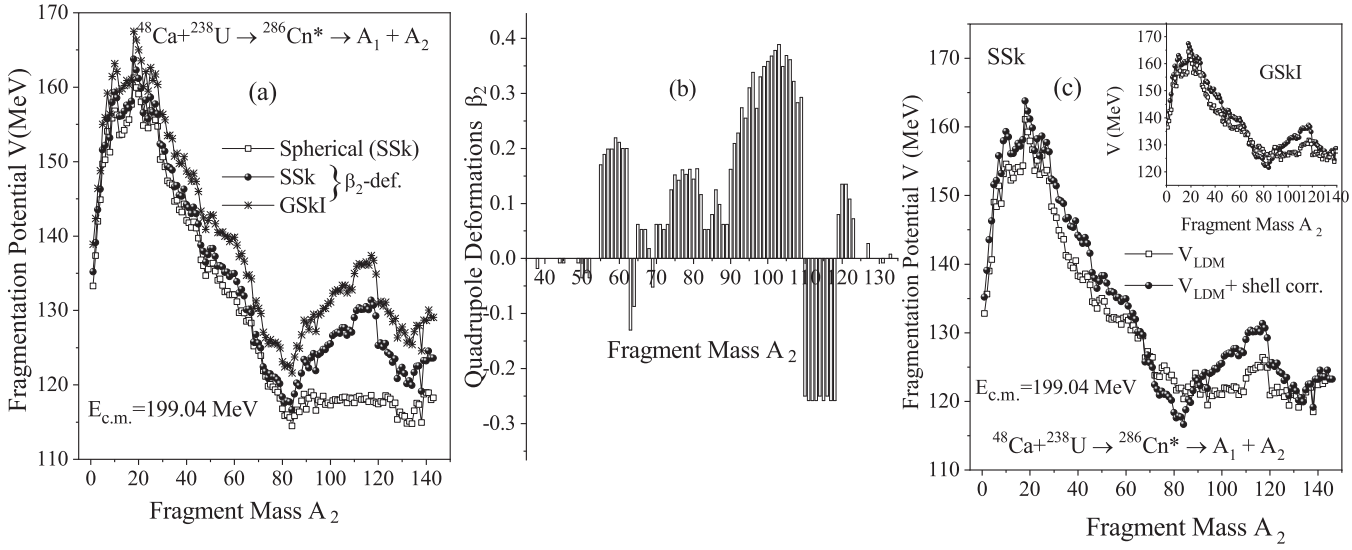

FIG. 3. (a) Variation of the fragmentation potential for spherical and deformed approach. For deformed fragmentation potential the GSkI and SSk forces are included (b) represents the variation of β_2-deformations with the fragment mass A_2 and (c) shows variation of the fragmentation potential with light fragment mass containing liquid drop part and liquid drop+shells corrections for SSk force. Inset shows the same result, but for GSkI force.

lower for the $A_2 = 84$–133 fragment mass range, which on the other hand get shifted towards higher magnitude when deformation and orientation effects are included. This suggests that the effect of the deformations drags the fragmentation of the above mentioned region towards the higher potential as compared to the spherical case, and becomes one of the reasons for the creation of the valley in the $A_2 = 73$–82 mass region for the deformed choice. The quadrupole deformations of decay fragments are also plotted on the y axis of the Fig. 3(b). The figure shows that the β_2 deformations are higher (up to 0.4 for prolate and -0.25 for oblate) for the $A_2 = 84$–133 mass region as compared to the other competing fragments. Hence, the larger magnitude of the deformations of the mentioned region causes the structure to deviate from the usual spherical path, i.e., the minima in the HMF region are mainly attributed to the high deformations of $A_2 = 84$–133 nuclei. Similar results are obtained for $^{292}Fl^*$ and $^{296}Lv^*$ nuclei, not reported here to avoid repetition.

The structure of the fragmentation potential for the decay of the $^{286}Cn^*$ compound nucleus is further investigated in terms of shell effects of the decaying fragments. Figure 3(c) represents the variation of the fragmentation potential with and without inclusion of the shell corrections (δU) using both SSk and GSkI (shown in inset) Skyrme forces. The open squares depict the fragmentation plot without considering the shell effects of the fragments and the filled circles represent the modified structure for V_{LDM} + shell corrections. It is evident from the figure that the fragmentation potential V (MeV) shows differences in the magnitude and structure for the $A_2 = 73$–82 mass region after inclusion of the shell effects. Another point of view of the shell effects is experienced by looking at the inset of Fig. 2(a). The valley in the mentioned region is governed through the extremely stable Pb isotopes (marked in the figure). The lower fragmentation potential around Pb leads to the minima in fragmentation structure in the $A_2 = 73$–82 region. It is relevant to mention that the fragmentation structures of $Z = 114$ and $Z = 116$ are not presented in Fig. 3, to avoid repetition, though same results are inferred for these nuclei as well. Hence Fig. 3 is sufficient to express the importance of the deformations and shell effects of the decaying fragments, responsible for the emergence of HMFs. In the previous analysis of DCM [19], the proximity based work also displayed HMF valleys similar to those in the present case, but with relatively lower magnitude. Moreover, the asymmetric decay is more prominent with the chosen Skyrme forces, and the contribution of asymmetric quasifission governed through the Pb valley soars upward as compared to the fission region (see Fig. 3(a) of [19]).

After discussing the role of Skyrme forces on barrier characteristics and fragmentation path, the study is further extended to address the total capture cross section using the considered forces. The capture cross section is a sum of compound nucleus fission+quasifission+evaporation residue cross sections [18]. Experimentally [18] it has been reported that the evaporation residue cross sections are of the order of picobarns, and the same are analyzed in the present work within the framework of the dynamical cluster-decay model (DCM). Table II is presented here to represent the neutron ($3n$ and $4n$) evaporation cross sections (σ_{ER}) of $^{286}Cn^*$, $^{292}Fl^*$, and $^{296}Lv^*$ nuclei at $E_{c.m} = 199$ to 206 MeV, calculated by including SSk and GSkI forces. The fixed values of the neck-length parameters ΔR and angular momentum states are also reported in Table II. On comparing the tabulated data for both Skyrme forces, the following points are observed: (i) Within DCM, both SSk and GSkI are capable of addressing the experimental ER data ($3n$ and $4n$) nicely for $Z = 112$, 114, and 116 superheavy nuclei. (ii) Higher neck length (ΔR) and lower ℓ values are required for the SSk force as compared to the GSkI force. Further to address the contribution of other events towards the capture cross sections, the fusion-fission

TABLE II. Experimental [18] and DCM fitted neutron evaporation cross sections of ^{286}Cn*, ^{292}Fl*, and ^{296}Lv* nuclei.

				ΔR (fm)		σ^{ER}_{DCM} (pb)		ℓ_{max} ($\hbar$)		
	Particle emitted	$E_{c.m.}$ (MeV)	T (MeV)	GSkI	SSk	GSkI	SSk	GSkI	SSk	$\sigma^{ER}_{Exp.}$ (pb)
^{286}Cn*	3n	195.04	1.178	2.305	2.54	2.59	3.0	75	69	$2.5^{+1.8}_{-1.1}$
	4n	199.04	1.224	2.442	2.67	0.60	0.51	78	74	$0.6^{+1.6}_{-0.5}$
^{292}Fl*	3n	196.50	1.167	2.235	2.473	0.55	0.55	64	60	$0.5^{+0.6}_{-0.3}$
	3n	201.50	1.246	2.240	2.470	3.6	3.10	66	62	$3.6^{+3.4}_{-1.7}$
	4n	201.50	1.246	2.464	2.694	4.77	4.7	69	66	$4.6^{+3.6}_{-1.9}$
^{296}Lv*	3n	199.47	1.109	2.256	2.530	0.64	0.46	57	54	$0.5^{+0.5}_{-0.3}$
	3n	206.40	1.222	2.164	2.410	1.25	1.2	62	58	$1.2^{+1.7}_{-0.8}$
	4n	206.40	1.222	2.462	2.615	3.17	3.5	65	61	$3.2^{+2.0}_{-1.2}$

and quasifission processes are also investigated. It is relevant to mention that the fission and quasifission data are handled explicitly through the SSk force, as the magnitude of the potential (see Figs. 1 and 2) associated with the GSkI force is not sufficient to address the fission and quasifission events. In view of this, Figure 4 is plotted to differentiate fusion-fission and quasifission events within the application of the SSk force. Figure 4 clearly shows the emergence of symmetric and asymmetric peaks. The symmetric distribution of the fragments primarily corresponds to the fusion fission (ff) process. However, the chances of symmetric quasifission ($QF_{sym.}$) also persist, as the magicity around tin (Sn) drives the composite system towards symmetric decay (collectively marked as the ff+$QF_{sym.}$ window in Fig. 4). Hence the symmetric mass distribution of the fragments can be governed through two decay modes: fusion-fission and symmetric quasifission. On the other hand, the asymmetric decay is associated with the Pb magicity, as discussed earlier. The peaks around Pb and the complementary fragments can be associated with the asymmetric quasifission process. In view of above discussion, the decay picture of $Z = 112$, 114, and 116 nuclei is quite visible through the mass distribution of the fragments. The figure assures that the disintegration of the superheavy nuclei is mainly governed through the compound (CN) and the noncompound nuclear (nCN) phenomena. It is important to mention that lower magnitude of the asymmetric peaks was reported in the previous work [19] (Prox-77) as compared to the symmetric events for the $Z = 112$ nucleus. This implies that symmetric fission is dominant as compared to the asymmetric distribution. However, the asymmetry in the structure increases with increase in Z number. Broadly speaking, the asymmetric quasifission component is higher for the ^{292}Fl* nucleus and further increases for the ^{296}Lv* nucleus. In comparison to the analysis of [19], a larger contribution of the asymmetric quasifission peaks is investigated for the SSk force (see Fig. 4) in the present work. Conclusively, the preformation probability of the asymmetric mode is significantly influenced with the use of the SEDF approach.

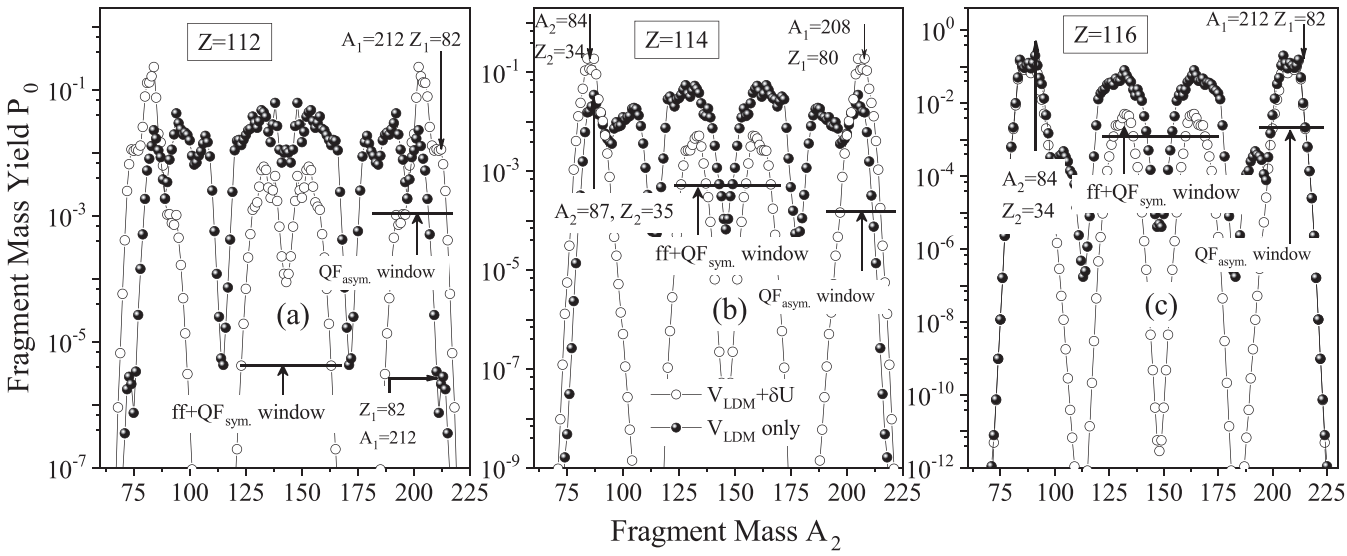

FIG. 4. Variation of mass yield P_0 as a function of fragment mass A_2, plotted using binding energy as liquid drop with shell corrections ($V_{LDM} + \delta U$) to the fragmentation potential, and also without shell corrections (V_{LDM}) of the fragments. The graph is plotted using the SSk force.

As mentioned earlier, the asymmetric quasifission is mainly governed through the magicity around the Pb peaks and the complementary fragments. Additionally, the shell corrections play a vital role in influencing the mass distribution, which is further required to distinguish the fusion-fission and quasifission processes. It is clearly evident from Fig. 4(a) that the preformation probability changes significantly when the shell corrections are added to the liquid drop potential. The preformation probability decreases with the inclusion of the shell corrections for the symmetric fission region. Moreover, the mass distribution gets asymmetrically peaked around the Pb region after their inclusion and gets wider if the shell effects are omitted. Hence, it is difficult to distinguish the different decay processes for the $Z = 112$ nucleus with $V_{\rm LDM}$ exclusively. In spite of symmetric decay, the magnitude of preformation probability shows an increment for the Pb ($Z = 82$, $A = 212$) peak with the inclusion of shell effects, shown by open circles in Fig. 4(a), which otherwise decreases in magnitude for the latter case. Hence this graph shows the significance of the shell corrections in the decay of the $Z = 112$ nucleus. Figures 4(b) and 4(c) are plotted to represent the preformation probabilities of ^{292}Fl* and ^{296}Lv* nuclei. Similar observations can be derived from these figures for the symmetric mass split. Moreover, if the magnitudes of the symmetric region of $Z = 112$, 114, and 116 nuclei are compared, then it is clearly visible that higher magnitude is observed for ^{296}Lv*, nucleus which gradually decreases for ^{292}Fl* and further for ^{286}Cn* nuclear systems. In contrast, the competition between symmetric and asymmetric modes can be analyzed for $Z = 114$ and 116 nuclear systems because their magnitudes are approximately the same, which otherwise show huge difference for the $Z = 112$ case, with the inclusion of the shell correction part. Some heavy mass fragments ranging $A_1 = 186$–200 also become part of the asymmetric mass fragmentation around Pb with the use of the liquid drop part. On the other hand, with the inclusion of shell corrections, the suppression in the preformation factor of these fragments occurs, which results in the strong peaked region around Pb isotopes for $Z = 112$, 114 and 116 superheavy nuclei. Hence the shell corrections play an immense role toward completing decay processes of superheavy nuclei.

Owing to the above discussion, the fusion-fission and quasifission crosssections (symmetric and asymmetric) are calculated and tabulated in Tables III to V. The experimental data for the asymmetric quasifission cross section ($\sigma^{\rm asym.QF}_{\rm Expt.}$) are obtained by subtracting the contribution of the symmetric cross section ($\sigma_{\rm CN\pm A/20}$), which is $\sigma_{\rm CN\pm A/20} = \sigma_{ff} + \sigma_{\rm sym.QF}$ from the capture cross section ($\sigma_{\rm cap}$). Moreover, the symmetric quasifission cross sections ($\sigma^{\rm sym.QF}_{\rm Expt.}$) are calculated as $\sigma^{\rm sym.QF}_{\rm Expt.} = \sigma_{\rm CN\pm A/20} - \sigma_{ff}$. It is evident from Tables II and IV that, to address the σ_{ff} and $\sigma^{\rm asym.QF}_{\rm Expt.}$ events, relatively higher magnitude of the neck-length parameters (above 2 fm) and lesser angular momentum values are required as compared to the previous DCM based work (see Table I of [19]). At these tabulated values, fusion-fission and asymmetric quasifission cross sections find nice agreement with the experimental work [18]. It is important to mention that the above tables are calculated by including the SSk force only, as the GSkI force does not fit the data of fission and quasifission processes (symmetric and asymmetric) within the DCM framework.

TABLE III. The fusion-fission (ff) cross sections fitted for the decay of ^{286}Cn*, ^{292}Fl*, and ^{296}Lv* nuclei formed in ^{48}Ca-induced reactions. The fitted values of ΔR and $\ell_{\rm max}$ are also given in the table along with the center-of-mass energies.

	$E_{\rm c.m.}$ (MeV)	T (MeV)	ΔR (fm)	$\sigma^{ff}_{\rm DCM}$ (mb)	$\ell_{\rm max}$ ($\hbar$)	$\sigma^{ff}_{\rm Expt.}$ [18] (mb)
^{286}Cn*	195.04	1.178	2.670	4.36	70	$\leqslant$4.2
	199.04	1.224	2.690	8.46	75	$\leqslant$9.2
^{292}Fl*	196.50	1.167	2.690	1.94	62	$\leqslant$2.2
	201.50	1.246	2.710	5.88	68	$\leqslant$6.0
^{296}Lv*	199.47	1.109	2.605	0.68	55	$\leqslant$0.7
	206.40	1.222	2.699	3.92	62	$\leqslant$4.0

Note that for fusion fission cross sections the conventional method of DCM is used, where P_0 is calculated by the collective clusterization technique in which relative preformation probability of all possible binary fragments is taken into account. The calculated probability then goes into Eq. (8) to calculate the fusion-fission cross sections for considered fragments. On the other hand, the asymmetric quasifission ($\rm QF_{asym.}$) cross sections are addressed by distributing $P_0 = 1$ among the fragments lying around the Pb peaks (marked as the $\rm QF_{asym.}$ window in Fig. 4). A similar procedure is adopted to account for the symmetric quasifission cross sections ($\rm QF_{sym.}$) as seen from Table IV. For the $\rm QF_{sym.}$ cross-section, the isotopes of Sn are minimized in the fragmentation process as $\rm QF_{sym.}$ is mainly governed through the Sn magicity and the preformation probability $P_0 = 1$ is distributed among these fragments. It is clearly seen from Table IV that the magnitude of cross sections for the symmetric quasifission process is underestimated for $Z = 112$ and $Z = 114$ nuclei; however, it shows better agreement for the $Z = 116$ nucleus. This leads to a fact that for ^{286}Cn* and ^{292}Fl* nuclear systems, the contribution of symmetric quasifission is feeble towards the capture cross sections. Hence $A_{\rm CN}/2 \pm 20$ is mainly associated with the fusion-fission phenomenon for these nuclei. This point can further be supported by Fig. 5 where the penetration probability is plotted as a function of fragment mass with SSk force. The figure clearly depicts that higher penetration probability is observed for 132–140 fragments. On the other hand, Sn

TABLE IV. The symmetric quasifission crosssections ($\sigma^{\rm sym.QF}$) are tabulated for $Z = 112$–116 nuclei. The center-of-mass energies and ΔR and $\ell_{\rm max}$ values are also presented in the table.

	$E_{\rm c.m.}$ (MeV)	T (MeV)	ΔR (fm)	$\sigma^{\rm sym.QF}_{\rm DCM}$ (mb)	$\ell_{\rm max}$ ($\hbar$)	$\sigma^{\rm sym.QF}_{\rm Expt.}$ [18] (mb)
^{286}Cn*	195.04	1.178	2.73	3.73	70	4.29
	199.04	1.224	2.71	3.75	75	31.3
^{292}Fl*	196.50	1.167	2.73	2.45	62	4.58
	201.50	1.246	2.715	3.19	68	9.0
^{296}Lv*	199.47	1.109	2.66	1.30	55	1.28
	206.40	1.222	2.7	2.77	62	2.67

TABLE V. Same as Table IV but results are shown for asymmetric quasifission events.

	$E_{\text{c.m.}}$ (MeV)	T (MeV)	ΔR (fm)	$\sigma_{\text{DCM}}^{\text{asym.QF}}$ (mb)	$\ell_{\max}$ ($\hbar$)	$\sigma_{\text{Expt.}}^{\text{asym.QF}}$ [18] (mb)
^{286}Cn*	195.04	1.178	2.780	103.0	70	101.78
	199.04	1.224	2.818	178.8	75	175.26
^{292}Fl*	196.50	1.167	2.675	46.60	62	44.750
	201.50	1.246	2.712	85.40	68	86.150
^{296}Lv*	199.47	1.109	2.638	27.60	55	28.730
	206.40	1.222	2.722	87.60	62	88.000

fragments associated with mass numbers 123–130 are less probable candidates for penetration, mainly for $Z = 112$ and 114 nuclei. In spite of having higher preformation probability for the fragments in the neighborhood of Sn, the corresponding penetration probability is much lower. This result further justifies that the contribution of the symmetric quasifission associated with the Sn magicity is less towards the capture cross section.

Further, Fig. 6 is plotted to account for the penetration probability of the asymmetric fragments at highest and lowest values of the center-of-mass energies. The figure clearly shows that the penetration probability of the fragments around Pb (and complementary fragments) lies in the range 0.1–0.6, while penetrability of fission fragments is within 0.1–1.0 (see Fig. 5). Hence, asymmetric quasifission and fission are the competing decay modes for $Z = 112$, 114, and 116 nuclei.

In the subsequent work, the fission cross sections are addressed again by considering the compound nucleus formation probability P_{CN}. Instead of using a clusterization procedure (discussed earlier) to address the fission fragments, the calculated P_{CN} is distributed among the fission fragments and the cross sections are calculated again within the DCM framework. Table VI illustrates the calculated values of compound nucleus preformation probability P_{CN} and the neck-length parameters for $Z = 112$, 114, and 116 nuclei at respective P_{CN} values. The formula used to calculate the P_{CN} is given by [40,41]

$$P_{\text{CN}}(E^*_{\text{CN}}, \ell) = \frac{1/\left[1 + \exp\frac{(x_m - \xi)}{\tau}\right]}{1 + \exp[(E_B - E^*_{\text{CN}})/\Delta]}. \tag{16}$$

Here E^*_{CN} is the excitation energy of the compound nucleus and E_B is the bass energy for the same. The values of parameters τ and ξ are defined as 0.0226 and 0.721 respectively [40]. Δ is the adjustable parameter of about 4 MeV. The mean fissility parameter (x_m) [40] is defined as the linear combination of the effective fissility parameter x_{eff} and compound nucleus fissility parameter x_{CN}, i.e., $x_m = 0.75x_{\text{eff}} + 0.25x_{\text{CN}}$. From Table VI it is observed that the calculated magnitude of P_{CN} for ^{286}Cn* nucleus is in the range of 0.09, which

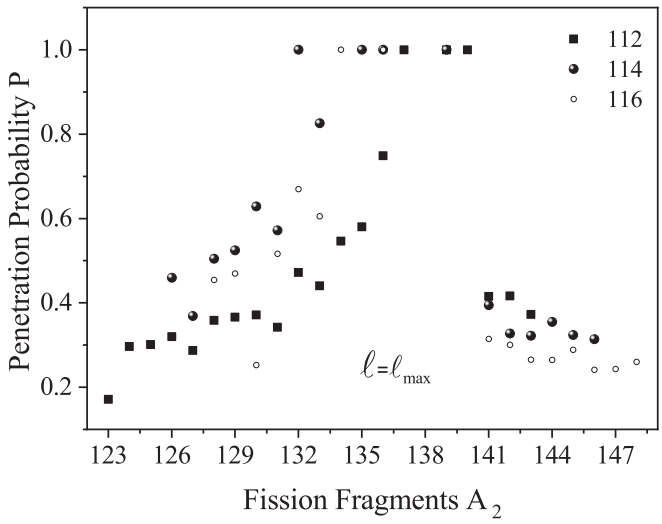

FIG. 5. Penetration probability P as a function of fission mass fragments plotted at $E_{\text{c.m.}} = 199$, 201, and 206 MeV respectively for $Z = 112$, 114, and 116 nuclei using SSk force.

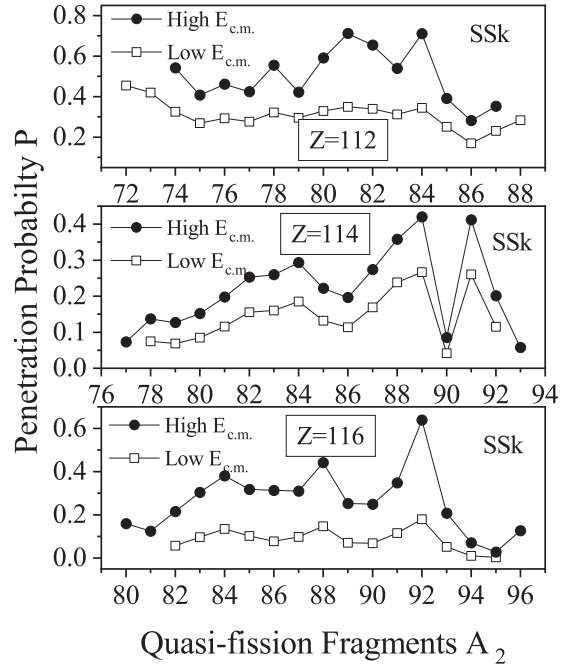

FIG. 6. The figure is same as the Fig. 5 but plotted for asymmetric quasifission fragments.

TABLE VI. The fission cross sections of $Z = 112$, 114, and 116 nuclear systems correspond to the P_{CN} values calculated through Eq. (16).

	$E_{\text{CN}} \pm 2$ (MeV)	ΔR (fm)	σ_{DCM} (mb)	$\sigma_{\text{Expt.}}$ (mb)	$\ell_{\max}$ ($\hbar$)	P_{CN}
^{286}Cn*	39	2.573	9.16	9.2	75	0.0960
	35	2.550	3.86	4.2	70	0.0917
^{292}Fl*	40	2.572	6.2	6.0	68	0.0649
	35	2.550	2.7	2.2	62	0.0593
^{296}Lv*	39	2.537	3.94	4.0	62	0.0432
	32	2.470	0.74	0.70	65	0.0368

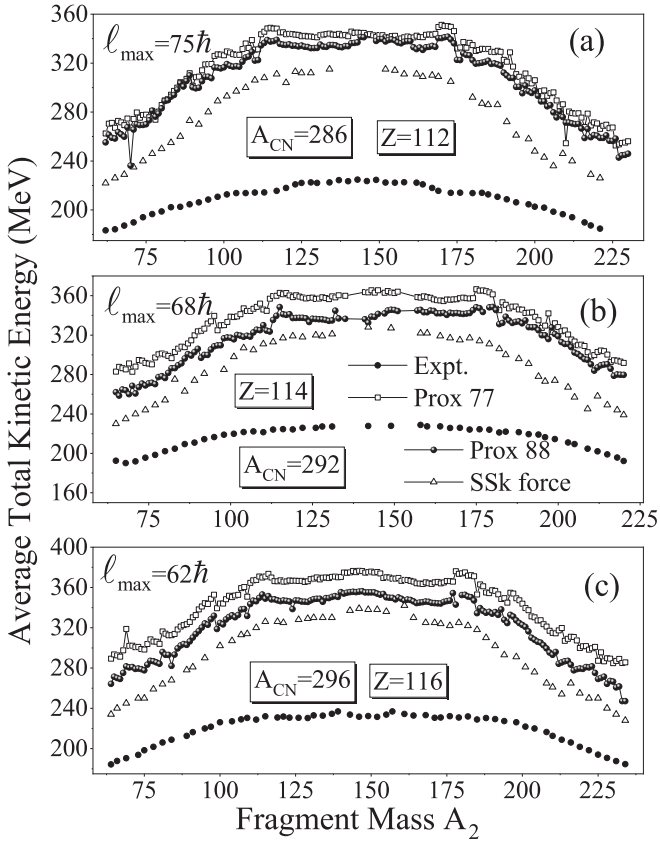

FIG. 7. Variation of average total kinetic energy distribution TKE as a function of fragment mass (A_2) plotted for $Z = 112$–116 nuclei with the SSk force and compared with Prox-77 and Prox-88 potentials [20,21].

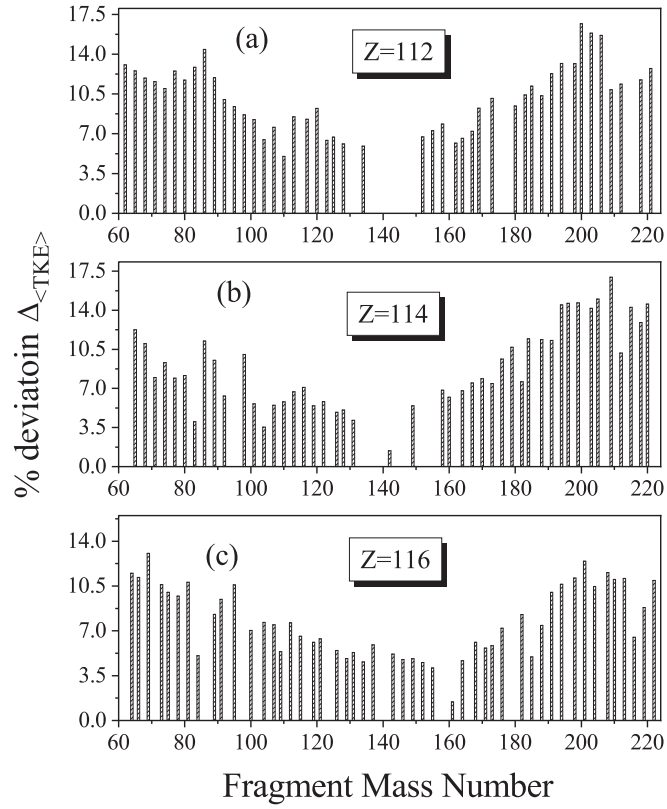

FIG. 8. Percentage deviation of average TKE calculated with the SSk force with respect to the Prox-88 potential [21].

further decreases to 0.06 and 0.04 respectively for ^{292}Fl* and ^{296}Lv* nuclei. This means that, with an increase in number of protons, the probability of compound nucleus formation decreases and noncompound nucleus decay (quasifission) starts competing, which is in accordance with an experimental result [18]. Moreover, at the calculated values of P_{CN}, the magnitude of the neck-length parameter (ΔR) shows a decrement by unit value as compared to Table III, estimated through the collective clusterization technique.

In conclusion, the above work is carried out to understand the role of SEDF in the dynamics of ^{48}Ca-induced reactions through fusion-fission and quasifission (symmetric and asymmetric) events. In the next section, the decay analysis is investigated further in terms of average TKE of CN-fission and quasifission components with SSk Skyrme force.

B. Average total kinetic energy (TKE) of CN-fission and quasifission components

The Skyrme energy density formalism is applied to study the average total kinetic energy (TKE) distribution of ^{286}Cn*, ^{292}Fl*, and ^{296}Lv* superheavy nuclei. In the previous analysis [19] various nuclear radii [42] were tested to explore average TKE values. The best results were predicted for $R_i = 1.233A_i^{1/3} - 0.978A_i^{-1/3}$ fm ($i = 1, 2$) radius parameter included in the Prox-88 potential. In view of [19], the present work is extended with an application of the SSk force instead of the proximity based potentials. In order to see the effect of both Blocki and SEDF based potentials on average TKE, Fig. 7 is plotted, where, in addition to the SSk force, the data from [19] are also included. It is important to mention here that Prox-77 and Prox-88 potentials are based on the phenomenological method, where simple mathematical formulas are used to describe the nuclear potential. However, in the SSk force a semiclassical macro-microscopic approach is used to estimate the same. Figures 7(a) to 7(c) depict that the average TKE significantly overestimates the experimental values even for the use of a Skyrme based nuclear potential, but the results with SEDF are relatively better as compared with Prox-77 and Prox-88 potentials. Therefore, it will be of future interest to employ the role of secondary particle emission and analyze its impact on average TKE distribution. To quantify the difference, the percentage deviation in average TKE for SSk force with respect to the Prox-88 potential is calculated and the same is depicted in Fig. 8. It is observed from the figure that the average kinetic energy drops to 18% for $Z = 112$ and $Z = 114$ nuclei and up to 14% for $Z = 116$ SHE in comparison to Prox-88, thereby indicating the significance of using the SEDF based potentials in the study of kinetic energy behavior of the superheavy elements. Along with this, the impact of spin-orbit density dependent potential V_J is also tested on the average kinetic energy distribution by plotting the graph of percentage change in average TKE ($\Delta\langle\text{TKE}\rangle\%$)

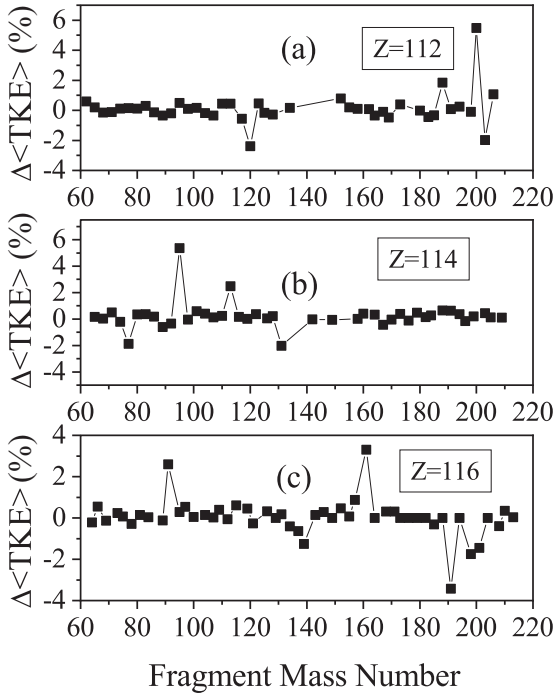

FIG. 9. Percentage deviation of average TKE calculated with and without the inclusion of spin-orbit dependent part V_J, calculated by using the SSk Skyrme force.

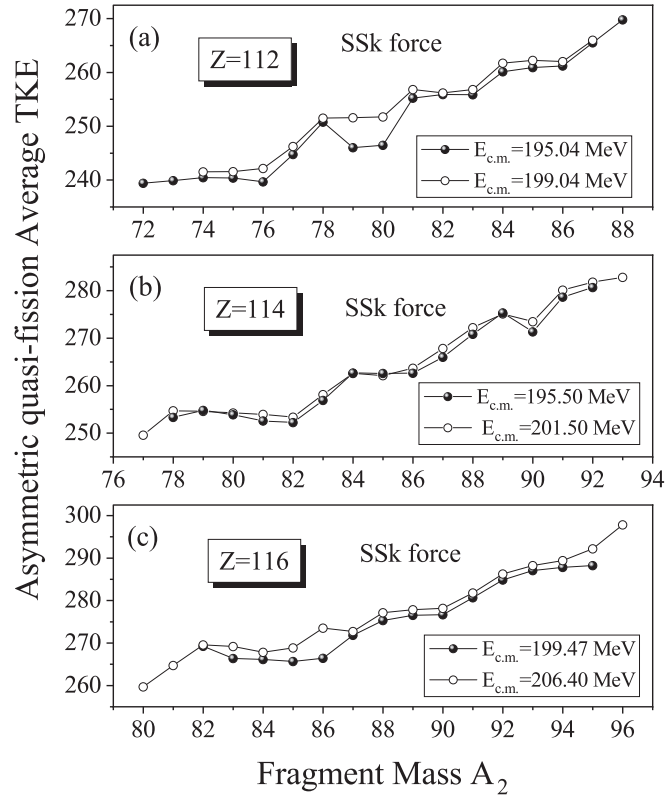

FIG. 10. Same as Fig. 7 but for asymmetric QF fragments.

with and without including V_J in the calculations. The results shown in Fig. 9 are obtained from the relation

$$\Delta\langle \mathrm{TKE}\rangle = \frac{\langle \mathrm{TKE}\rangle(V_P + V_J) - \langle \mathrm{TKE}\rangle(V_J)}{\langle \mathrm{TKE}\rangle(V_P + V_J)}.$$

It is observed from the figure that exclusion of the V_J part from the nuclear potential leads to deviation in the theoretical and experimental average TKE values, as $\Delta\langle \mathrm{TKE}\rangle\%$ shows significant fluctuations. The change in average TKE is up to 5% for $Z = 112$, 114, and 116 superheavy systems.

Finally the average TKE of asymmetric quasifission fragments is estimated using the SSk force and results are shown in Fig. 10. The average TKE is plotted at lowest and highest $E_{\mathrm{c.m.}}$ values. The calculations indicate that the average TKE of asymmetric quasifission fragments does not change much with center-of-mass energy. It means that the full dissipation of energy occurs in the $\mathrm{QF}_{\mathrm{asym.}}$ process and the energy excess is introduced into the system and transformed to intrinsic excitation of fragments.

IV. SUMMARY

The dynamics of ^{286}Cn*, ^{292}Fl*, and ^{296}Lv* superheavy nuclei is studied using the Skyrme energy density formalism (SEDF) within the dynamical cluster decay model. In the present analysis, two different Skyrme forces, namely GSkI and SSk, having distinct barrier characteristics, are considered to address the ^{48}Ca-induced reactions. Using SEDF, the capture cross sections, which include ER, fission, and QF (symmetric and asymmetric), are calculated by using the neck-length parameter (ΔR) of the model. The calculations suggest that SSk force is able to address the complete capture data; however, the GSkI force is suitable exclusively for the neutron evaporation channel. The mass distribution of fission fragments shows symmetric (fusion-fission and symmetric quasifission) peaks along with the dominance of asymmetric quasifission. Furthermore, the distribution of average total kinetic energy of decay fragments is estimated. Relatively better results are shown for the density dependent SSk force in comparison to previously used density independent potentials (such as Prox-77 and Prox-88). However, calculated average TKE with the SSk force still shows significant overestimation with respect to the experimental data. Therefore it will be of future interest to see the impact of secondary particle emission on average TKE distribution.

ACKNOWLEDGMENTS

This work is supported by the Council of Scientific and Industrial Research (CSIR), New Delhi [Files No. 09/0677(11733)/2021-EMR-I and No. 09/1007(13391)/2022-EMR-I] and a minor project grant (Letter No. KCP/2020/MS/2186-2191) made available from the G.S.S.D.G.S Khalsa College Patiala Research Fund.

[1] Yu. Ts. Oganessian, J. Phys. G **34**, R165 (2007).
[2] S. Hofmann and G. Münzenberg, Rev. Mod. Phys. **72**, 733 (2000).
[3] K. Morita *et al.*, J. Phys. Soc. Jpn. **73**, 1738 (2004).
[4] Y. T. Oganessian, V. K. Utyonkov, Y. V. Lobanov, F. S. Abdullin, A. N. Polyakov, I. V. Shirokovsky, Y. S. Tsyganov, G. G. Gulbekian, S. L. Bogomolov, B. N. Gikal, A. N. Mezentsev, S. Iliev, V. G. Subbotin, A. M. Sukhov, A. A. Voinov, G. V. Buklanov, K. Subotic, V. I. Zagrebaev, M. G. Itkis, J. B. Patin *et al.*, Phys. Rev. C **70**, 064609 (2004).
[5] J. Randrup, P. Möller, and A. J. Sierk, Phys. Rev. C **84**, 034613 (2011).
[6] J. Randrup and P. Möller, Phys. Rev. C **88**, 064606 (2013).
[7] Y. Aritomo and S. Chiba, Phys. Rev. C **88**, 044614 (2013).
[8] V. Zagrebaev and W. Greiner, J. Phys. G: Nucl. Part. Phys. **31**, 825 (2005).
[9] Y. Aritomo, K. Hagino, K. Nishio, and S. Chiba, Phys. Rev. C **85**, 044614 (2012).
[10] C. Simenel, Eur. Phys. J. A **48**, 152 (2012).
[11] B. B. Singh, M. K. Sharma, and R. K. Gupta, Phys. Rev. C **77**, 054613 (2008); M. K. Sharma, S. Kanwar, G. Sawhney, R. K. Gupta, and W. Greiner, J. Phys. G: Nucl. Part. Phys. **38**, 055104 (2011).
[12] R. K. Gupta, in *Cluster in Nuclei*, Lecture Notes in Physics 818, edited by C. Beck, Vol. I (Springer-Verlag, Berlin, 2010), p. 223.
[13] R. K. Gupta, S. K. Arun, R. Kumar, and M. Bansal, Nucl. Phys. A **834**, 176c (2010).
[14] Rajni, R. Kumar and M. K. Sharma, Phys. Rev. C **90**, 044604 (2014).
[15] R. Mittal, D. Jain, and M. K. Sharma, Nucl. Phys. A **968**, 436 (2017).
[16] G. Kaur, K. Sandhu, and M. K. Sharma, Nucl. Phys. A **971**, 95 (2018).
[17] G. Kaur and M. K. Sharma, Nucl. Phys. A **990**, 79 (2019).
[18] E. M. Kozulin, G. N. Knyazheva, I. M. Itkis, M. G. Itkis, A. A. Bogachev, E. V. Chernysheva, L. Krupa, F. Hanappe, O. Dorvaux, L. Stuttge, W. H. Trzaska, C. Schmitt, and G. Chubarian, Phys. Rev. C **90**, 054608 (2014).
[19] G. Kaur, K. Sandhu, and M. K. Sharma, Phys. Rev. C **94**, 014615 (2016).
[20] J. Błocki, J. Randrup, W. J. Swiatecki, and C. F. Tsang, Ann. Phys. (NY) **105**, 427 (1977).
[21] W. Reisdorf, J. Phys. G: Nucl. Part. Phys. **20**, 1297 (1994).
[22] W. D. Myers and W. J. Swiatecki, Phys. Rev. C **62**, 044610 (2000).
[23] D. Vautherin, Phys. Rev. C **7**, 296 (1973).
[24] D. Rajni, I. Sharma, and M. K. Sharma, Eur. Phys. J A **53**, 208 (2017).
[25] B. K. Agrawal, S. K. Dhiman, and R. Kumar, Phys. Rev. C **73**, 034319 (2006).
[26] J. Bartel and K. Bencheikh, Eur. Phys. J. A **14**, 179 (2002).
[27] D. Jain, R. Kumar, M. K. Sharma, and R. K. Gupta, Phys. Rev. C **85**, 024615 (2012).
[28] R. K. Gupta, D. Singh, R. Kumar, and W. Greiner, J. Phys. G: Nucl. Part. Phys. **36**, 075104 (2009).
[29] J. Maruhn and W. Greiner, Phys. Rev. Lett. **32**, 548 (1974).
[30] R. K. Gupta, W. Scheid, and W. Greiner, Phys. Rev. Lett. **35**, 353 (1975).
[31] A. Săndulescu, R. K. Gupta, W. Scheid, and W. Greiner, Phys. Lett. B **60**, 225 (1976).
[32] K. J. LeCouteur and D. W. Lang, Nucl. Phys. **13**, 32 (1959).
[33] G. Audi and A. H. Wapstra, Nucl. Phys. A **595**, 409 (1995).
[34] P. Möller, J. R. Nix, W. D. Myers, and W. J. Swiatecki, At. Data Nucl. Data Tables **59**, 185 (1995).
[35] L. R. B. Elton, *Nuclear Sizes* (Oxford University Press, London, 1961).
[36] H. de Vries, C. W. de Jager, and C. de Vries, At. Data Nucl. Data Tables **36**, 495 (1987).
[37] Niyti, A. Deep, R. Kharab, S. Chopra, and R. K. Gupta, Phys. Rev. C **95**, 034602 (2017).
[38] N. J. Davidson, S. S. Hsiao, J. Markram, H. G. Miller, and Y. Tsang, Nucl. Phys. A **570**, 61 (1994).
[39] W. Myers and W. J. Swiatecki, Nucl. Phys. A **81**, 1 (1966).
[40] E. M. Kozulin, G. N. Knyazheva, K. V. Novikov, I. M. Itkis, M. G. Itkis, S. N. Dmitriev, Y. T. Oganessian, A. A. Bogachev, N. I. Kozulina, I. Harca, W. H. Trzaska, and T. K. Ghosh, Phys. Rev. C **94**, 054613 (2016).
[41] V. I. Zagrebaev and W. Greiner, Nucl. Phys. A **944**, 257 (2015).
[42] I. Dutt and R. K. Puri, Phys. Rev. C **81**, 064609 (2010); **81**, 064608 (2010).